Nanoscale

PAPER

View Article Online
View Journal | View Issue

Cite this: *Nanoscale*, 2026, **18**, 7789

Reticular assembly of 1D and 2D Cu_{10} cluster-assembled materials as a recyclable luminescent probe for highly sensitive creatinine detection

Tsukasa Irie, † Riki Nakatani,† Sreelakshmi K. S.,† Kohki Sasaki, Mika Nozaki, Ayumu Kondo, Tokuhisa Kawawaki, Saikat Das * and Yuichi Negishi *

Atomically precise metal cluster–assembled materials provide a powerful platform for engineering modular photophysical responses through well-defined cluster–linker interfaces. Here we report two copper cluster-assembled materials (CCAMs), **Cu_{10}-bddi** and **Cu_{10}-dptp**, obtained through the reticular integration of a decanuclear copper cluster with either a linear diisonicotinate linker (bddi) or a π-extended thiophene–dipyridyl linker (dptp). Single-crystal X-ray diffraction reveals distinct coordination chemistries: **Cu_{10}-bddi** features a Cu(I)-rich cluster bridged by thiolate and carboxylate donors to generate 1D chains, whereas **Cu_{10}-dptp** incorporates N-donor linkers to stabilize a Cu(I)-rich cluster environment assembled into fully extended 2D sheets. X-ray photoelectron spectroscopy corroborates these oxidation-state assignments and highlights the differing electronic structures of the two frameworks. Both CCAMs exhibit permanent microporosity arising from periodic cluster packing, enabling efficient molecular access to the luminescent cluster nodes. Optical studies disclose linker-to-cluster–coupled absorption features and distinct emission signatures in water. These properties render the materials effective luminescent probes for creatinine, an essential biomarker for kidney function. **Cu_{10}-bddi** undergoes strong fluorescence quenching upon creatinine binding, attributable to efficient photoinduced electron or energy transfer within its confined 1D channels. Conversely, **Cu_{10}-dptp** displays emission enhancement, consistent with rigidity-induced suppression of nonradiative decay within its 2D π-extended environment. Both sensing processes follow Stern–Volmer behavior and afford low detection limits. Importantly, each CCAM demonstrates excellent recyclability over fifteen sensing cycles, with FT-IR confirming structural integrity. This work shows that reticular Cu_{10} cluster assembly enables robust, reusable luminescent sensors and underscores how oxidation state, dimensionality, and pore architecture govern aqueous analyte recognition.

Received 13th December 2025,
Accepted 9th March 2026

DOI: 10.1039/d5nr05249a

rsc.li/nanoscale

Introduction

Atomically precise metal nanoclusters (NCs) represent a distinctive class of matter in which discrete electronic states, molecularly defined metal–ligand coordination, and sub-3 nm core dimensions converge to produce photophysical and chemical behaviors inaccessible to larger nanoparticles.[1–20] Their quantized energy levels, abundant surface sites, and rich redox flexibility have enabled advances in luminescence sensing, biological imaging, and chemical detection.[21–27] Among the various NC systems, copper nanoclusters (Cu NCs) are particularly compelling owing to the earth abundance, low toxicity, and versatile oxidation-state chemistry of Cu, combined with their intrinsic propensity for strong ligand–metal charge interactions.[28–33] Yet, the practical deployment of Cu NCs in sensing applications remains limited by their notorious instability: discrete Cu clusters readily undergo oxidation, ligand loss, and structural rearrangement, which leads to rapid degradation of emissive properties and reduced reproducibility in aqueous or biological environments.

A powerful strategy to overcome these limitations is reticular cluster assembly, in which atomically precise NCs are immobilized and spatially organized into extended architectures through coordination bonding with organic linkers.[34–36] Transforming discrete clusters into cluster-assembled materials (CAMs) suppresses many degradation pathways by constraining cluster mobility, reinforcing metal–ligand bonds, and distributing mechanical and chemical stress across a periodic lattice.[37–47] In addition, reticular assembly introduces new structural degrees of freedom—framework dimensionality, pore geometry, and connectivity—that cannot be accessed

Institute of Multidisciplinary Research for Advanced Materials, Tohoku University, Aoba-ku, Sendai 980-8577, Japan. E-mail: das.saikat.c4@tohoku.ac.jp, yuichi.negishi.a8@tohoku.ac.jp
† These authors contributed equally.

in isolated NCs and that directly influence analyte diffusion, host–guest interactions, and photophysical modulation. From a sensing perspective, CAMs offer several intrinsic advantages: (i) well-defined binding pockets that modulate analyte access to the emissive cluster node; (ii) immobilization of chromophoric linkers that enhances electronic communication between linkers and cluster-based excited states; (iii) improved structural robustness, ensuring reproducible luminescence responses over multiple cycles; and (iv) the ability to engineer analyte-responsive behavior by tuning nodal charge density, ligand field strength, and metal coordination environment.

Despite these conceptual advantages, systematic control over the dimensionality and electronic structure of Cu-based CAMs (CCAMs)[48–51] remains extremely underdeveloped, and its consequences for luminescence sensing are poorly understood. In particular, the interplay between framework dimensionality (one-dimensional, 1D, *vs.* two-dimensional, 2D), the cluster's local coordination geometry and electronic microenvironment (ligand field strength, donor set, and degree of metal–ligand/metal–metal coupling), and linker electronics has not been thoroughly exploited to modulate photophysical responses or host–guest interactions. No prior study has demonstrated how decisive variations in cluster coordination environment and reticular topology can be leveraged to tune both *direction* and *magnitude* of the sensing response toward clinically relevant analytes. Creatinine, an essential renal function biomarker, represents a stringent test case for luminescent sensor design due to its zwitterionic nature, moderate polarity, and strong hydrogen-bonding propensity.[52] Effective detection platforms must therefore combine (i) accessible pore environments, (ii) tunable microenvironments for analyte binding, and (iii) photophysically responsive cluster nodes capable of undergoing quenching or enhancement upon guest interaction. CCAMs offer a uniquely ideal platform for this purpose, yet their application to creatinine sensing has never been explored.

In this study, we introduce two structurally distinct CCAMs—**Cu_{10}-bddi**, a 1D chain architecture assembled from the linear diisonicotinate linker but-2-yne-1,4-diyl diisonicotinate (bddi), and **Cu_{10}-dptp**, a 2D sheet architecture constructed using the π-extended thiophene–dipyridyl linker 2,5-di(pyridin-4-yl)thiophene (dptp). Single-crystal X-ray diffraction reveals fundamentally different decanuclear cluster environments: in **Cu_{10}-bddi**, the $Cu(I)_{10}$ core is encapsulated by a compact thiolate–carboxylate coordination shell, with pyridyl linkers serving primarily as intercluster connectors to generate rigid 1D chains that favor localized cluster-centered electronic states, whereas in **Cu_{10}-dptp** the $Cu(I)_{10}$ cluster is directly incorporated into a mixed S/O/N-donor coordination environment and periodically bridged by π-extended pyridyl linkers to form electronically coupled 2D sheets with enhanced delocalization. These variations in coordination geometry, donor environment, and degree of electronic coupling collectively dictate the materials' photoluminescence profiles and their divergent luminescence responses upon creatinine binding—fluorescence quenching in **Cu_{10}-bddi** and emission enhancement in **Cu_{10}-dptp**. By rationally tuning the dimensionality, coordination environment, and electronic structure of the Cu_{10} cluster node, we establish a structurally grounded framework for designing responsive, robust, and recyclable luminescent sensors. The insights gained here demonstrate how reticular cluster assembly can be systematically exploited to encode analyte–framework interactions and excited-state dynamics, paving the way for next-generation luminescent sensing platforms.

Results and discussion

Both **Cu_{10}-bddi** and **Cu_{10}-dptp** were synthesized under mild solution conditions through controlled ligand-exchange at a preformed thiolate-protected $[CuS^tBu]_n$ precursor. Upon protonolysis with trifluoroacetic acid, the *in situ*–generated Cu_{10} cluster cores undergo reticular assembly with either the diisonicotinate (bddi) or thiophene-dipyridyl (dptp) linker, yielding block-shaped 1D **Cu_{10}-bddi** crystals and elongated prismatic 2D **Cu_{10}-dptp** crystals at the phase boundary. These solvothermal-free crystallizations afford phase-pure CCAMs in moderate isolated yields (Fig. 1). Single-crystal X-ray crystallography

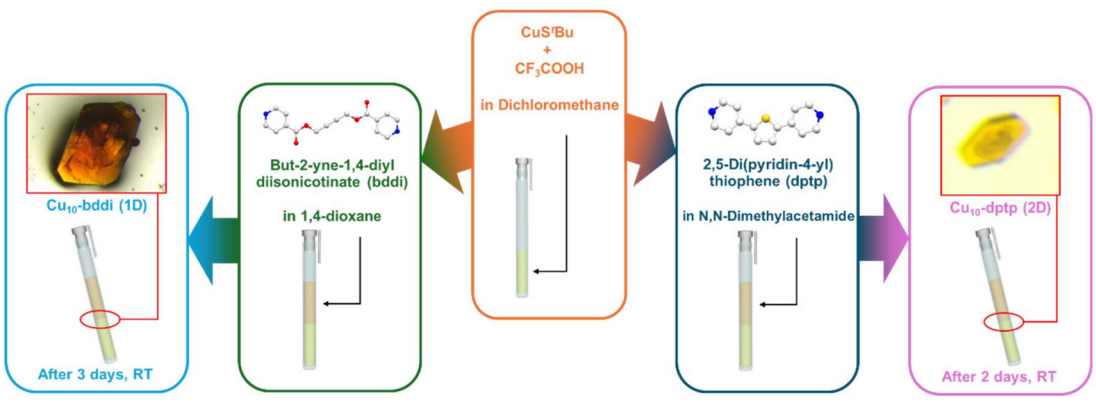

Fig. 1 Schematic illustration of the synthetic route affording single crystals of **Cu_{10}-bddi** and **Cu_{10}-dptp**, accompanied by optical micrographs of crystals collected at the immiscible liquid–liquid interface. Color scheme: N, blue; S, yellow; O, red; C, gray. H atoms are omitted for clarity.

reveals that **Cu_{10}-bddi** is constructed from an atomically well-defined decanuclear copper cluster (Fig. S1) that functions as a rigid SBU and assembles into an extended 1D coordination polymer through the ditopic organic linker bddi. The crystal adopts space group $P\bar{1}$ (Table S1); the crystallographic asymmetric unit (ASU) contains five crystallographically distinct Cu sites (Cu1–Cu5) which, by inversion symmetry, are reproduced to give the full Cu_{10} node. The Cu_{10} node is therefore best described as a centrosymmetric dimer of two Cu_5 subunits that are mutually connected through the coordinated ligand shell described later (Fig. 2a and S2). The metal core contains ten Cu atoms arranged as two symmetry-related Cu_5 motifs that together form an elongated decanuclear scaffold. Intermetallic separations within the Cu10 node are relatively short and tightly distributed: Cu···Cu distances span 2.6507(8)–2.8382(8) Å (representative short contacts: Cu4–Cu5 = 2.6507(8) Å; Cu1–Cu2 = 2.7469(9) Å) (Table S3). These short Cu···Cu separations are indicative of significant metal–metal adjacency (frequently referred to as cuprophilic contacts in multinuclear copper systems) that contribute to electronic coupling between metal centers. Nevertheless, the Cu_{10} motif is best described as an assembly of distinct coordination centers (with mixed local geometries) stabilized by ligand bridging and a limited set of short Cu···Cu adjacencies, rather than a single compact metallic cage with uniform metal–metal bonding. Individual Cu centers display a variety of local coordination environments (from lower coordination where short Cu···Cu contacts or terminal ligands occur, to four- or five-coordinate geometries where carboxylate, thiolate and pyridyl donors converge), giving rise to square-planar, square-pyramidal and distorted tetrahedral site geometries across the node. The inorganic core is capped and partially bridged by *tert*-butylthiolate (S^tBu^-) ligands (Fig. 2b). The asymmetric unit contains three independent S atoms (S1–S3); inversion symmetry yields six S donors per Cu_{10} node (Fig. S3). The Cu–S distances span 2.171(1)–2.598(1) Å, reflecting a spectrum of coordination modes from short, strongly bound thiolate linkages to longer, semi-coordinative interactions (Table S4). Representative short Cu–S contacts include S3–Cu5 = 2.171(1) Å; S2–Cu5 = 2.186(1) Å; S1–Cu3 = 2.219(1) Å; S1–Cu4 = 2.215(1) Å, while the longer end of the distribution (up to 2.598(1) Å) corresponds to more weakly interacting S···Cu contacts that are symmetry-related or occur in second-coordination environments. In the Cu_5 motif some thiolates adopt μ-bridging character (μ_2 and, by symmetry relations, higher effective bridging multiplicities), whereas other S atoms are essentially terminal. The collection of μ-bridging and terminal thiolates generates a Cu–S network at the cluster periphery that (i) sterically protects the core by virtue of the bulky *tert*-butyl groups, (ii) stabilizes the copper centers through soft S donation, and (iii) mediates connectivity within the Cu_5 subunits. Trifluoroacetate (CF_3COO^-) anions contribute essential structural stabilization within the Cu_{10} secondary building unit. The ASU contains two crystallographically independent CF_3COO^- ligands, which, by inversion symmetry, furnish a total of four carboxylates per Cu_{10} node (Fig. 2c and S4). Analysis of Cu–O bonding geometries reveals a mixed carboxylate coordination manifold, comprising both μ_2-η^1:η^1 bridging and monodentate/chelating interactions, consistent with the structural roles commonly observed in high-nuclearity copper clusters. One CF_3COO^- ligand adopts a μ_2-η^1:η^1 bridging mode, in which the two oxygen atoms coordinate to two different Cu centers, thereby linking adjacent Cu sites across the Cu_5 subunit. The Cu–O distances for this asymmetric bridge are O1–Cu1 = 2.072(4) Å and O2–Cu2 = 2.128(4) Å, which are consistent with μ_2-bridging carboxylate coordination commonly observed in multinuclear copper cluster frameworks (Table S5). In contrast, the second carboxylate exhibits non-bridging behavior, acting through a single Cu–O interaction. A representative short terminal Cu–O contact, O7–Cu4 = 1.981(4) Å, defines this coordination environment; the absence of a second nearby Cu–O interaction in this region indicates that the ligand functions as a monodentate or κ^2-chelate (depending on the secondary O-donor geometry), but not as a bridging group.

This terminal/chelating ligand helps enforce the observed square-planar or square-pyramidal configurations at selected Cu sites. Overall, the set of μ_2-bridging and terminal/chelating carboxylates forms a compact equatorial Cu–O envelope around the cluster. The bridging CF_3COO^- units knit together neighboring Cu atoms within the Cu_5 halves of the Cu_{10} node, whereas the terminal/chelating carboxylates fine-tune the local geometries of surface-exposed copper atoms. The strongly elec-

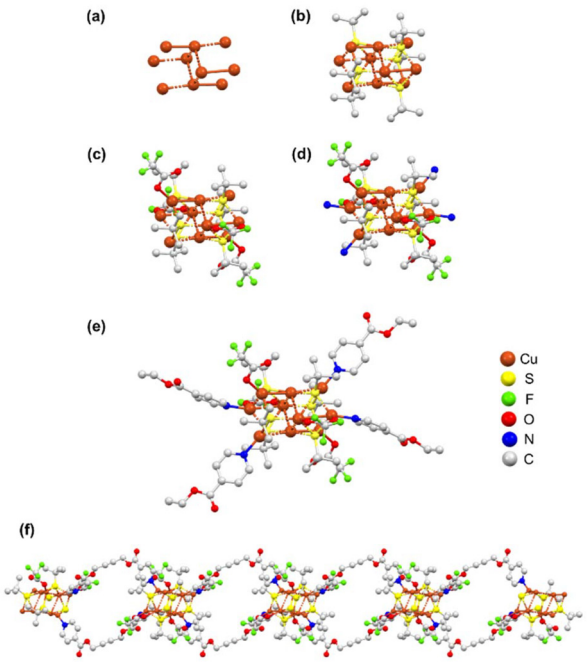

Fig. 2 Stepwise construction of the Cu_{10} NC node in **Cu_{10}-bddi**: (a) the Cu_{10} core, followed by sequential incorporation of (b) S^tBu ligands, (c) CF_3COO^- ligands, and (d) the organic linkers. (e) The fully ligated Cu_{10} unit serves as a 4-connected node coordinating four bddi molecules. (f) Each Cu_{10} node is connected to two neighboring nodes *via* two bddi linkers on each side, generating a robust, linear 1D coordination polymer. H atoms are omitted for clarity.

tron-withdrawing CF_3 substituents attenuate the donor strength of the carboxylate oxygen atoms, thereby modulating both the Lewis acidity and the electronic distribution across the ten copper atoms (five crystallographically independent Cu sites generated by inversion symmetry). The organic linker bddi is a rigid, linear ditopic pyridyl-terminated linker. The asymmetric unit contains two crystallographically independent pyridyl nitrogen atoms (N1 and N2) that coordinate to copper centers at N1–Cu2 = 2.013(4) Å and N2–Cu3 = 1.989(4) Å (Fig. 2d, S5 and Table S6). Because each bddi ligand is ditopic and lies across an inversion center, the two N atoms in the ASU correspond to one full bddi linker. In total, inversion symmetry generates four bddi linkers per Cu_{10} node (two bound at Cu2 and two at Cu3) (Fig. 2e). The four bddi linkers are arranged as two approximately colinear pairs so that each neighboring Cu_{10} node is bridged by two parallel bddi linkers, producing a double-rod connection between adjacent clusters along a single crystallographic direction. Each Cu_{10} node is therefore linked to two immediate neighbors on opposite sides by two bddi linkers on each side, and the aggregate connectivity yields a robust, strictly 1D coordination polymer (Fig. 2f).

The crystal structure of **Cu_{10}-dptp** (Table S2) features a neutral decanuclear copper cluster that acts as the inorganic node of the coordination framework. Ten crystallographically related Cu centers (five crystallographically independent sites, Cu1–Cu5, in space group $P2_1/c$) assemble into a compact $\{Cu_{10}S_6O_6N_4\}$ core (Fig. S6) constructed from μ_2-/μ_3-thiolate, a combination of bridging and terminal carboxylate ligation, and peripheral pyridyl coordination from dptp. Within the cluster, the Cu···Cu separations fall in the range 2.657(3)–2.838(3) Å (Fig. 3a, S7 and Table S7), characteristic of thiolate/carboxylate-bridged Cu(I) aggregates and indicative of a tightly knit metal core. Each copper center adopts a distorted coordination environment defined by a mixture of S, O, and N donors. The Cu–S bond lengths lie in the range 2.150(4)–2.560(4) Å (*e.g.*, Cu1–S1 = 2.210(4) Å, Cu2–S1 = 2.165(4) Å, Cu3–S2 = 2.250(4) Å, Cu3–S3 = 2.560(4) Å), reflecting μ_2-/μ_3-bridging thiolate coordination around the metal belt. The Cu–O carboxylate contacts are relatively short, with three distinct Cu–O interactions per asymmetric unit: Cu1–O(terminal) = 2.02(2) Å and Cu3–O(bridging) = 2.043(9) Å, Cu4–O(bridging) = 2.100(9) Å. These distances are fully consistent with strong Cu–O carboxylate coordination in mixed bridging/terminal modes. The Cu–N pyridyl bonds are also in the expected range, Cu–N = 1.97(1)–2.02(1) Å (Cu5–N2 = 1.97(1) Å, Cu4–N1 = 2.02(1) Å), corresponding to terminal pyridyl donors from the dptp linkers. Taken together, the ten copper centers and their S/O/N ligation define a robust, charge-balanced $\{Cu_{10}S_6O_6N_4\}$ cluster, which can be topologically treated as a 4-connected node in the extended framework. The thiolate shell of the Cu_{10} core is composed of *tert*-butylthiolate (S^tBu^-) ligands. In the asymmetric unit, three crystallographically independent thiolate S atoms (S1–S3) are present, which generate a total of six thiolate ligands per Cu_{10} cluster when symmetry is taken into account (Fig. 3b and S8). These sulfur donors adopt a combination of μ_2- and μ_3-bridging modes: S1 bridges multiple copper centers in a μ_3 fashion, coordinating to Cu1, Cu2, and Cu3/Cu4 (*e.g.*, Cu1–S1 = 2.210(4) Å, Cu2–S1 = 2.165(4) Å, Cu3–S1 = 2.445(5) Å, Cu4–S1 = 2.277(5) Å), thereby capping a Cu_3/Cu_4 fragment within the cluster (Table S8). The Cu–S–Cu angles around S1 span approximately 70–125°, consistent with a μ_3-thiolate geometry. S2 acts as a μ_2/μ_3 bridge linking Cu1, Cu3, and Cu5 (Cu1–S2 = 2.218(5) Å, Cu3–S2 = 2.250(4) Å, Cu5–S2 = 2.221(5)

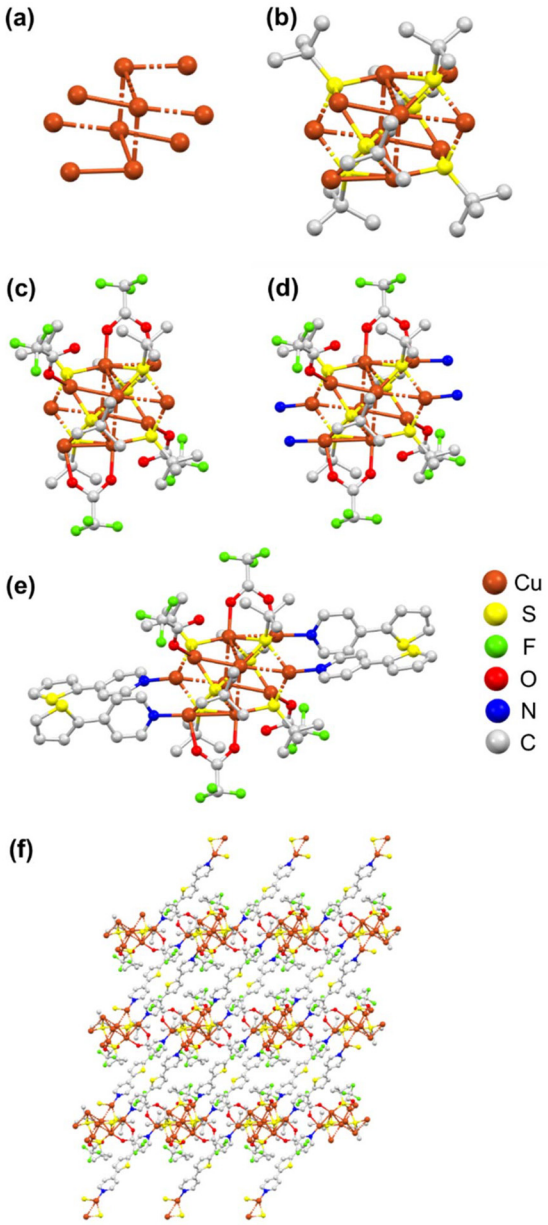

Fig. 3 Stepwise assembly of the Cu_{10} NC node in **Cu_{10}-dptp**: (a) the Cu_{10} core, followed by addition of (b) S^tBu ligands, (c) CF_3COO^- ligands, and (d) the organic linkers. (e) The fully ligated Cu_{10} cluster functions as a 4-connected node bound to four dptp molecules. (f) Each Cu_{10} node is connected to four neighboring nodes through four dptp linkers, generating an extended 2D coordination sheet. The resulting topology corresponds to a distorted (4,4)-type net in which Cu_{10} nodes are periodically arranged and bridged by nearly linear dptp linkers. H atoms are omitted for clarity.

Å), further stitching together the copper belt. S3 similarly adopts a μ_3-bridging mode between Cu2, Cu3, Cu4, and Cu5 (Cu2–S3 = 2.150(4) Å, Cu3–S3 = 2.560(4) Å, Cu4–S3 = 2.319(4) Å, Cu5–S3 = 2.252(3) Å), reinforcing the multinuclear connectivity. Collectively, the six S^tBu^- ligands (per Cu_{10} unit) furnish a hydrophobic, sterically encumbered thiolate shell that encapsulates the Cu_{10} core, stabilizes the aggregation, and fine-tunes the local electronic environment of the copper centers. The *tert*-butyl groups project outward from the core, playing an important role in governing the packing and interlayer interactions in the 2D framework. The carboxylate shell is built from CF_3COO^- anions. Two crystallographically distinct CF_3COO^- ligands are present in the asymmetric unit, which, under space-group symmetry, generate the full carboxylate complement around the Cu_{10} node (Fig. 3c). Crucially, the single-crystal X-ray crystallography shows that only three independent Cu–O carboxylate bonds occur per asymmetric unit: a bridging CF_3COO^- ligand (centered at C4) binds in a μ_2-κO:κO fashion, with its two oxygen atoms coordinating to different copper centers: one O atom binds Cu3 (Cu3–O3 = 2.043(9) Å), and the other O atom binds Cu4 (Cu4–O1 = 2.100(9) Å) (Fig. S9 and Table S9). This ligand thus ties Cu3 and Cu4 together through a syn–syn bridging mode, as reflected in the C4–O–Cu angles (C4–O3–Cu3 = 125(1)°, C4–O1–Cu4 = 121(1)°). A second CF_3COO^- ligand (centered at C2) adopts a monodentate κO terminal coordination mode, with one oxygen bound to Cu1 (Cu1–O7 = 2.02(2) Å) and the second oxygen (O015) non-coordinating (C2–O015 = 1.40(5) Å, with no Cu–O015 contact in the Cu–O bond list). This clearly distinguishes a terminal carboxylate (Cu1–O7 in the labeling) from the μ_2-bridging one (O1/O3). Symmetry expansion of these ligands around the Cu_{10} unit yields a total of six Cu–O carboxylate interactions per cluster, consistent with the $\{Cu_{10}S_6O_6N_4\}$ core formulation. Thus, the carboxylate shell consists of a mixture of μ_2-bridging CF_3COO^- (*via* two O donors to different Cu centers) and κO-terminal CF_3COO^- ligands, which together complete the O-donor environment of the Cu_{10} cluster and, in concert with S^tBu^-, ensure charge balance and structural rigidity. The outer coordination sphere of the Cu_{10} cluster is decorated by dptp, which acts as a rigid, π-conjugated N-donor linker (Fig. 3d). Each dptp molecule incorporates two terminal 4-pyridyl groups and a central thiophene ring. In the solid state: only the pyridyl N atoms coordinate to Cu centers: N1 binds to Cu4 (Cu4–N1 = 2.02(1) Å) and N2 binds to Cu5 (Cu5–N2 = 1.97(1) Å), giving rise to monodentate Cu–N pyridyl coordination (Fig. 3e, S10 and Table S10). The thiophene S atom (S4) does not coordinate to copper (it is bonded only to the organic carbon framework: S4–C22 and S4–C25 = 1.69(2) Å), and therefore serves purely as a structural and electronic component of the π-linker rather than a metal-binding site. Each dptp linker thus bridges two Cu_{10} clusters in a bis(monodentate) fashion, with the two pyridyl termini anchoring onto different decanuclear nodes. From a topological perspective, each Cu_{10} cluster behaves as a 4-connected node, linked to four neighboring clusters through four dptp linkers. This generates an extended 2D coordination sheet, in which Cu_{10} nodes are periodically arrayed and interconnected by nearly linear dptp spacers to form a distorted (4,4)-type net (Fig. 3f). The central thiophene unit enhances the rigidity and π-conjugation of the linker, promoting ordered packing and potential π–π interactions between adjacent organic backbones within a layer. The resulting **Cu_{10}-dptp** framework is strictly 2D in terms of coordination connectivity: strong Cu–S, Cu–O, and Cu–N pyridyl bonds define robust sheets, whereas interactions between neighboring layers are dominated by van der Waals contacts among the *tert*-butyl groups, CF_3 groups, and aromatic (pyridyl/thiophene) moieties. A least-squares plane fitted through the Cu_{10} cluster centers and their coordinated dptp linkers defines well-ordered lamellar sheets stacked along the direction approximately normal to this plane. From the crystallographic metrics, the interlayer distance, defined as the separation between adjacent **Cu_{10}-dptp** sheets along the stacking direction (*i.e.*, the centroid-to-centroid spacing between parallel **Cu_{10}-dptp** planes), is approximately 5.0 Å. This relatively short spacing reflects efficient packing and weak interlayer π–π and van der Waals contacts, while still preserving the integrity and accessibility of the Cu_{10} cluster nodes within the 2D lattice.

A comprehensive suite of analytical techniques was employed to elucidate the structural, compositional, morphological, and thermal features of the CCAMs **Cu_{10}-bddi** and **Cu_{10}-dptp**. Powder X-ray diffraction (PXRD) measurements confirm that both **Cu_{10}-bddi** and **Cu_{10}-dptp** crystallize as phase-pure materials. The experimentally obtained PXRD patterns exhibit excellent agreement with the simulated patterns generated from single-crystal X-ray diffraction (SCXRD) data (Fig. 4a and 5a), with all major reflections precisely reproduced and without the appearance of impurity peaks or diffuse scattering. The absence of peak broadening further attests to the high crystalline order and uniformity of the bulk samples. These results verify that the decanuclear Cu_{10} cluster units propagate periodically in both frameworks to yield long-range ordered 1D chains in **Cu_{10}-bddi** and 2D layers in **Cu_{10}-dptp**. Nitrogen sorption analyses were performed at 77 K following activation at 50 °C for 8 h. Both materials display Type-I isotherms (Fig. 4b and 5b), characterized by steep uptake at low relative pressures ($P/P_0 < 0.01$), indicating the presence of permanent microporosity despite their low-dimensional structural motifs. Although **Cu_{10}-bddi** consists of 1D cluster-based chains, measurable porosity arises from interchain free volume. The sterically bulky S^tBu^- and bddi linkers prevent tight packing of adjacent chains, creating microporous voids between them. These channels do not originate from intrinsic framework pores but rather from corrugated interchain spacing governed by the three-dimensional arrangement of the S^tBu^- groups and the orientation of bddi linkers. As a result, N_2 can access these extrinsic voids upon activation, yielding a moderate BET surface area of 47.0 $m^2\ g^{-1}$ (Fig. S11). This phenomenon is well established for low-dimensional metal–organic frameworks (MOFs) or cluster polymers in which steric hindrance and inefficient packing generate measurable surface areas despite their topological dimensionality. In con-

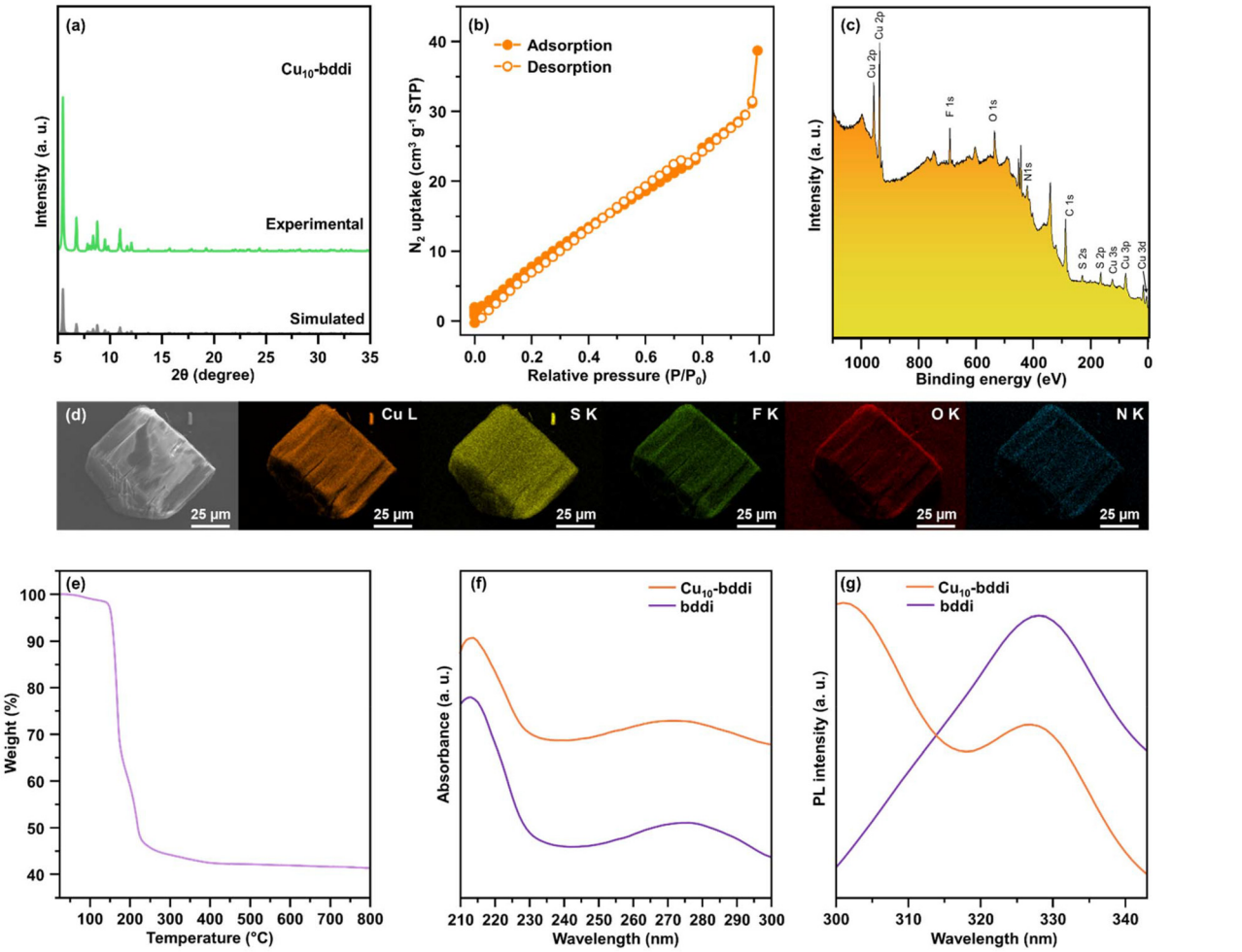

Fig. 4 (a) Comparison of simulated and experimental XRD patterns verifying the crystalline integrity of **Cu_{10}-bddi**. (b) N_2 adsorption–desorption isotherms collected at 77 K. (c) XPS survey spectrum revealing the surface elemental composition. (d) SEM image of **Cu_{10}-bddi** with corresponding EDX elemental maps illustrating the spatial distribution of individual elements. (e) TGA profile of **Cu_{10}-bddi** under a N_2 atmosphere; (f) UV–Vis absorption spectrum of **Cu_{10}-bddi** in water; and (g) photoluminescence emission profile of **Cu_{10}-bddi** in water under 275 nm excitation.

trast, **Cu_{10}-dptp** features a 2D coordination framework in which decanuclear Cu_{10} nodes are periodically bridged by rigid dptp linkers. The planarity and extended π-conjugation of the dptp linker restrict interlayer collapse, producing well-defined microporous galleries between the stacked 2D sheets. Furthermore, the bulkier CF_3COO^- and S^tBu^- ligands surrounding the Cu_{10} core generate intrinsic intralayer cavities, permitting additional adsorption pathways. Consequently, **Cu_{10}-dptp** exhibits a significantly higher BET surface area (137.8 $m^2\ g^{-1}$), consistent with expectations that 2D cluster-based frameworks retain more accessible void space than 1D chain-like analogues. XPS analysis provided detailed insights into elemental composition and oxidation states. Survey spectra confirmed the presence of Cu, S, N, O, C, and F in **Cu_{10}-bddi** and **Cu_{10}-dptp**, consistent with the Cu_{10} cluster core, thiolate and carboxylate ligands, and organic linkers (Fig. 4c and 5c). The Cu $2p_{3/2}$ and Cu $2p_{1/2}$ peaks of **Cu_{10}-bddi** appear at 932.3 eV and 952.2 eV, respectively (Fig. S13a), consistent with Cu(I)-centered copper environments. The S 2p peaks (162.2–163.3 eV) correspond to metal-bound thiolate (S^{2-}), while the higher-energy components at 167.3–168.5 eV arise from oxidized sulfur species, likely surface-bound sulfate or thiolate oxidation products—typical for Cu–thiolate cluster surfaces exposed to ambient conditions (Fig. S13b). The C 1s deconvolution shows peaks at 284.7 eV (C–C/C=C), 288.0 eV (O–C=O), and 290.6–295.3 eV (CF_3-related carbon), correlating to the bddi linker, carboxylates, and CF_3COO^- groups (Fig. S13c). The Cu 2p region of **Cu_{10}-dptp** shows peaks at 932.7 eV, 944.8 eV, and 952.5 eV (Fig. S14a). Crucially, the Cu $2p_{3/2}$ peak at 932.7 eV is characteristic of Cu(I). No shake-up satellites are observed—consistent with the diamagnetic $3d^{10}$ configuration of Cu(I). The S 2p spectrum again shows thiolate S^{2-} (162.2–163.3 eV) and trace oxidized sulfur (167.3–168.5 eV). The C 1s peak at 284.7 eV corresponds to the aromatic backbone of dptp. Together, the low Cu 2p binding energy, absence of satellite structure, and Auger features decisively establish

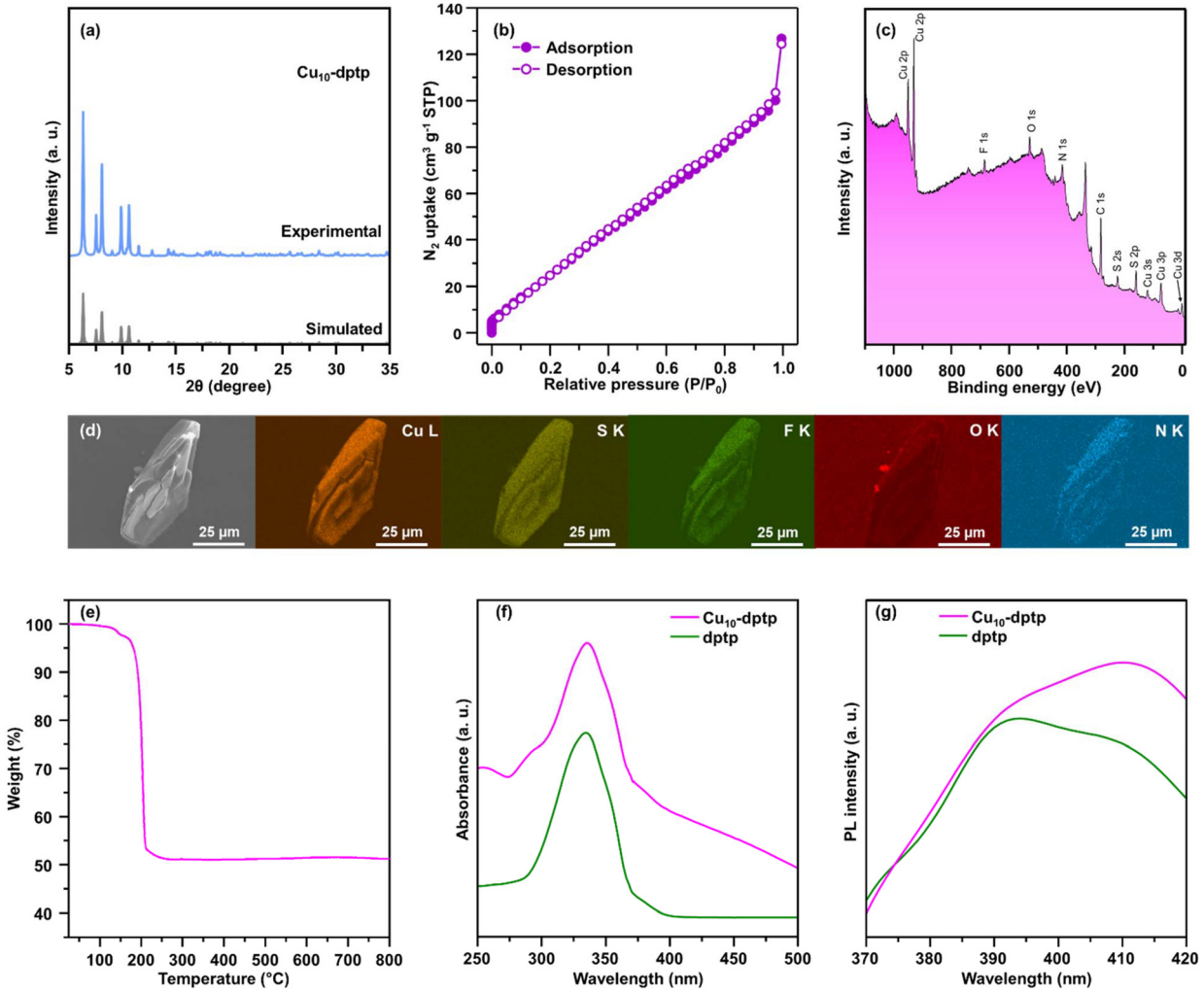

Fig. 5 (a) Comparison of simulated and experimental XRD patterns verifying the crystalline integrity of **Cu_{10}-dptp**. (b) N_2 adsorption–desorption isotherms collected at 77 K. (c) XPS survey spectrum revealing the surface elemental composition. (d) SEM image of **Cu_{10}-dptp** with corresponding EDX elemental maps illustrating the spatial distribution of individual elements. (e) TGA profile of **Cu_{10}-dptp** under a N_2 atmosphere; (f) UV–Vis absorption spectrum of **Cu_{10}-dptp** in water; and (g) photoluminescence emission profile of **Cu_{10}-dptp** in water under 355 nm excitation.

that the Cu_{10} clusters in **Cu_{10}-dptp** adopt a Cu(I) oxidation state. Scanning electron microscopy (SEM) revealed distinct habits for the two CCAMs: well-faceted block-like microcrystals for **Cu_{10}-bddi** and elongated prismatic crystals reflecting the anisotropic 2D sheet stacking for **Cu_{10}-dptp** (Fig. 4d and 5d). Energy-dispersive X-ray spectroscopy (EDX) elemental mapping showed homogeneous distributions of Cu, S, N, O, and F throughout the crystals, confirming uniform incorporation of all ligands and the absence of phase segregation. Thermogravimetric analysis (TGA) shows both CAMs exhibit good thermal robustness. **Cu_{10}-bddi** remains stable up to *ca.* 150 °C, while the 2D **Cu_{10}-dptp** framework exhibits improved stability, maintaining structural integrity up to *ca.* 180 °C (Fig. 4e and 5e). The enhanced stability of **Cu_{10}-dptp** is attributed to its 2D cluster-linked architecture, which provides greater lattice rigidity than the 1D chain arrangement in **Cu_{10}-bddi**. Together, these results validate that both frameworks are robust, crystalline, compositionally faithful CAMs whose properties emerge directly from their dimensionality and the steric/electronic environments defined by their organic linkers.

Optical spectroscopic analyses were carried out to gain insight into the electronic structures and emissive behavior of the CCAMs, and to elucidate how reticulation of organic chromophores within Cu_{10} cluster nodes modifies their photophysical response relative to the free linkers. UV–vis absorption and photoluminescence (PL) measurements were conducted both in aqueous dispersion and in the solid state to differentiate intrinsic molecular transitions from cluster-induced perturbations. These studies enable evaluation of (i) ligand-centered *versus* cluster-perturbed transitions, (ii) exciton localization/delocalization within the CCAM architecture, and (iii) the influence of metal–ligand coordination on radiative relaxation pathways. The UV–vis spectrum of **Cu_{10}-bddi** in water

displays a sharp absorption band at 213 nm and a broad band centered at 275 nm (Fig. 4f). These features originate from ligand-centered $\pi \rightarrow \pi^*$ transitions within the bddi linker: (i) the 213 nm transition corresponds to $\pi \rightarrow \pi^*$ excitation of the aromatic isonicotinate rings. (ii) The 275 nm band arises from the extended π-system including the conjugated alkyne (–C≡C–) bridge, whose electronic density is perturbed upon Cu–carboxylate coordination. Remarkably, the free bddi linker exhibits absorption maxima at 213 nm and 275 nm—identical to those observed for the cluster. This energy coincidence demonstrates that the Cu_{10} cluster acts as a structurally supporting but electronically non-intrusive scaffold in aqueous medium, imposing minimal modification to the intrinsic frontier orbitals of the linker. The absence of additional low-energy visible absorption suggests that the $Cu(I)_{10}$ cluster core does not introduce strong metal-centered or metal-to-ligand charge-transfer transitions in solution, consistent with its largely closed-shell electronic character. In the solid state, **Cu_{10}-bddi** exhibits a sharper absorption at 220 nm and two additional shoulders at 276 nm and 382 nm (Fig. S15). Relative to the free linker—which displays peaks at 213, 279, 430, and 510 nm—the following changes are observed: (i) blue-shifting of high-energy $\pi \rightarrow \pi^*$ transitions (213 → 220 nm) indicates slight framework-induced electronic confinement; (ii) the appearance of a shoulder at 382 nm reflects cluster-perturbed $\pi \rightarrow \pi^*$ transitions and weak interfacial charge-transfer coupling enabled by rigidification within the 1D chain architecture; and (iii) the broad linker-based absorptions at 430 and 510 nm in free bddi become suppressed upon cluster assembly, indicating quenching of low-energy intraligand charge-transfer pathways when the ligand is locked in a metal-coordinated environment. These results highlight that solid-state packing amplifies interchromophore coupling and reduces structural relaxation, thereby altering the accessible excited-state manifold. Upon excitation at 275 nm, aqueous **Cu_{10}-bddi** displays two emission maxima at 301 nm and 328 nm (Fig. 4g), whereas the free bddi linker shows only a single emission at 328 nm. This splitting arises from: (i) a ligand-centered $\pi \rightarrow \pi$ relaxation* at 328 nm, common to both linker and cluster, and (ii) an additional higher-energy emission at 301 nm resulting from rigidification of the bddi moiety within the Cu_{10} coordination framework, which suppresses vibrational dissipation and stabilizes a higher-lying emissive state. Thus, Cu_{10} cluster assembly opens an additional radiative channel not present in the isolated linker, consistent with the formation of structurally constrained 1D cluster–ligand chains. The UV–vis spectrum of **Cu_{10}-dptp** in water features a dominant absorption band at 335 nm (Fig. 5f), corresponding to the $\pi \rightarrow \pi^*$ excitation of the conjugated thiophene–pyridyl system. The lack of additional low-energy absorption indicates that the Cu(I) cluster nodes contribute minimally to ground-state optical transitions in solution, functioning primarily as electronically passive structural anchors. Strikingly, the free dptp linker exhibits an identical absorption maximum at 335 nm, indicating that: (i) the Cu(I) cluster exerts minimal perturbation on the linker's π-system in aqueous medium, and (ii) the metal centers primarily serve as structural anchoring sites rather than strong chromophoric contributors. In the solid state, **Cu_{10}-dptp** shows a sharp absorption at 248 nm and shoulders at 281 nm, 330 nm, and 377 nm (Fig. S16). Compared to the free linker, which absorbs at 273 nm, 329 nm, and 421 nm, several key differences emerge: (i) blue shifts at high energies (273 → 248 nm) reflect interlayer packing and reduced conformational freedom within the 2D framework; (ii) the presence of multiple shoulders suggests exciton delocalization across the 2D cluster–ligand sheet; and (iii) the suppression of the 421 nm linker band highlights quenching of intraligand charge-transfer states upon reticulation into the Cu_{10} cluster environment. These changes are consistent with the π-stacked 2D array of **Cu_{10}-dptp**, where the planarity and rigidity of dptp enhance transition coupling relative to the 1D **Cu_{10}-bddi** system. Excitation at 355 nm produces two emissions: a shoulder at 391 nm and a dominant peak at 410 nm (Fig. 5g). In contrast, the free dptp linker exhibits a prominent band at 394 nm and a shoulder at 410 nm. The red-shifted and intensity-reordered emission profile in the cluster material originates from: (i) enhanced conjugation and rigidity in the 2D **Cu_{10}-dptp** sheet, which stabilizes lower-energy excited states; (ii) cluster-assisted exciton delocalization, which promotes emission from a more extended π-manifold; and (iii) reduced solvent relaxation effects due to dense framework packing. The retention of the 410 nm shoulder in both systems highlights a common ligand-centered excited state, but the strengthened 391 → 410 nm transition in the cluster underscores the framework-induced modulation of emissive decay paths. Across both materials, comparison with the free linkers reveals: (i) minimal perturbation of $\pi \rightarrow \pi^*$ transitions in solution, demonstrating that the Cu_{10} clusters do not significantly alter ground-state orbital energies; (ii) pronounced solid-state modifications, including peak shifts and shoulder formation, arising from metal-assisted rigidification and packing-triggered exciton coupling; and (iii) distinct PL signatures, where **Cu_{10}-bddi** gains an additional emission (301 nm) due to 1D rigidification, and **Cu_{10}-dptp** exhibits red-shifted dual emission due to 2D delocalization and cluster-mediated electronic communication. These observations collectively demonstrate that coordination topology, framework dimensionality, and cluster–ligand electronic coupling govern the excited-state landscapes of Cu_{10}-based CCAMs.

Creatinine is an essential biomarker for assessing renal function, with abnormal creatinine levels serving as an early indicator of kidney dysfunction, metabolic imbalance, and muscle degradation. Fluorescence-based sensing offers a powerful route for creatinine detection owing to its high sensitivity, rapid response, and suitability for aqueous physiological media. Motivated by these factors, we evaluated the luminescent responses of two structurally distinct CCAMs—**Cu_{10}-bddi**, a 1D chain framework, and **Cu_{10}-dptp**, a 2D layered material—to establish how their cluster nuclearity, ligand field, and dimensionality govern molecular recognition and signal transduction in water. Both CCAMs incorporate Cu_{10} cluster nodes, but differ fundamentally in (i) their coordination connectivity

(1D *vs.* 2D), (ii) organic linker electronics (alkyne–isonicotinate *vs.* thiophene–dipyridyl systems), and (iii) the local coordination microenvironment and degree of cluster–ligand electronic coupling imposed by the reticular architecture. These differences translate into distinct excited-state landscapes and intermolecular interaction modes. The bddi linker features π-accepting isonicotinate groups and a rigid alkyne spacer, yielding spatially isolated Cu(I) cluster nodes embedded within compact coordination shells that favor localized cluster-centered and ligand-perturbed excited states highly sensitive to environmental quenching. In contrast, the dptp linker provides a π-rich thiophene core and strongly conjugated pyridyl termini that integrate Cu(I) clusters into extended 2D networks, promoting enhanced exciton delocalization and rigidity-assisted radiative decay. Together, these two CCAMs constitute an ideal testbed for understanding how framework dimensionality, linker polarizability, and coordination topology govern molecular sensing.

Upon incremental addition of creatinine (1.98×10^{-5}–4.28×10^{-4} M) to aqueous suspensions of **Cu_{10}-bddi** under λ_{ex} = 275 nm, the emission intensity decreased monotonically (Fig. 6a). The quenching behavior is attributed to adsorbate-induced perturbation of localized Cu(I) cluster–ligand excited states within the rigid 1D coordination framework, which enhances nonradiative relaxation through vibrational coupling and interfacial energy dissipation. Creatinine contains an elec-

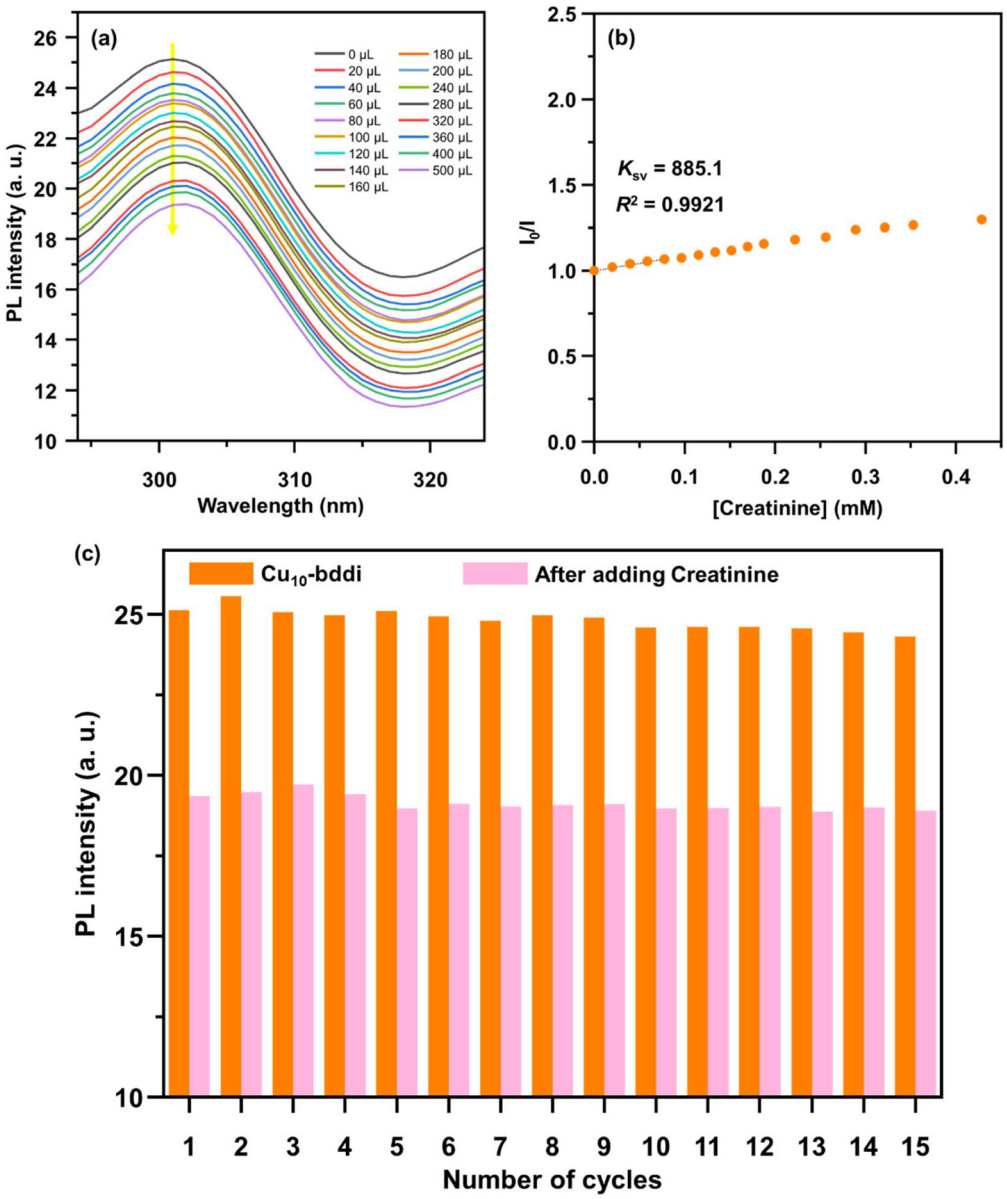

Fig. 6 (a) Concentration-dependent photoluminescence response of **Cu_{10}-bddi** to creatinine. (b) Stern–Volmer analysis illustrating fluorescence quenching behavior in aqueous media. (c) Reusability assessment of **Cu_{10}-bddi** over multiple creatinine sensing cycles.

tron-rich imidazolone moiety and carbonyl donors, enabling strong interactions with the outer coordination sphere of the Cu10 cluster, including hydrogen bonding to carboxylate oxygen atoms, dipolar electrostatic interactions within the polar Cu–O-rich microenvironment, and close outer-sphere contacts with surface-exposed Cu(I) sites. These interactions facilitate excited-state energy dissipation, leading to efficient quenching. In the low-concentration Stern–Volmer regime (1.98×10^{-5}–7.79×10^{-5} M), the linear relationship $I_0/I = 885.1$ [Q] + 1.00 (R^2 = 0.9921) indicates a dynamic quenching process, yielding a K_{SV} of 885.1 M^{-1} (Fig. 6b). The relatively large K_{SV} reflects the high accessibility of the Cu_{10} cluster nodes within the interchain free volume of the 1D architecture and the strong sensitivity of localized emissive states to guest-induced microenvironmental perturbation. The calculated limit of detection (LOD) of 726 μM demonstrates effective sensing performance within relevant physiological ranges and is notably lower than those reported for Au–Ag bimetallic nanoparticle-based sensors (800 μM)[53] and DNA aptamer–AuNP conjugate assays (870 μM).[54]

Remarkably, **Cu_{10}-dptp** exhibits an opposite trend: under λ_{ex} = 355 nm, the emission intensity increases with rising creatinine concentration (Fig. 7a). This enhancement originates from the Cu(I) cluster–assisted excited-state delocalization and rigidity of the 2D π-extended framework, which suppresses nonradiative decay pathways. Cu(I) cluster frameworks typically support cluster-centered and cluster–ligand-coupled excited states that are highly sensitive to framework rigidity and dielec-

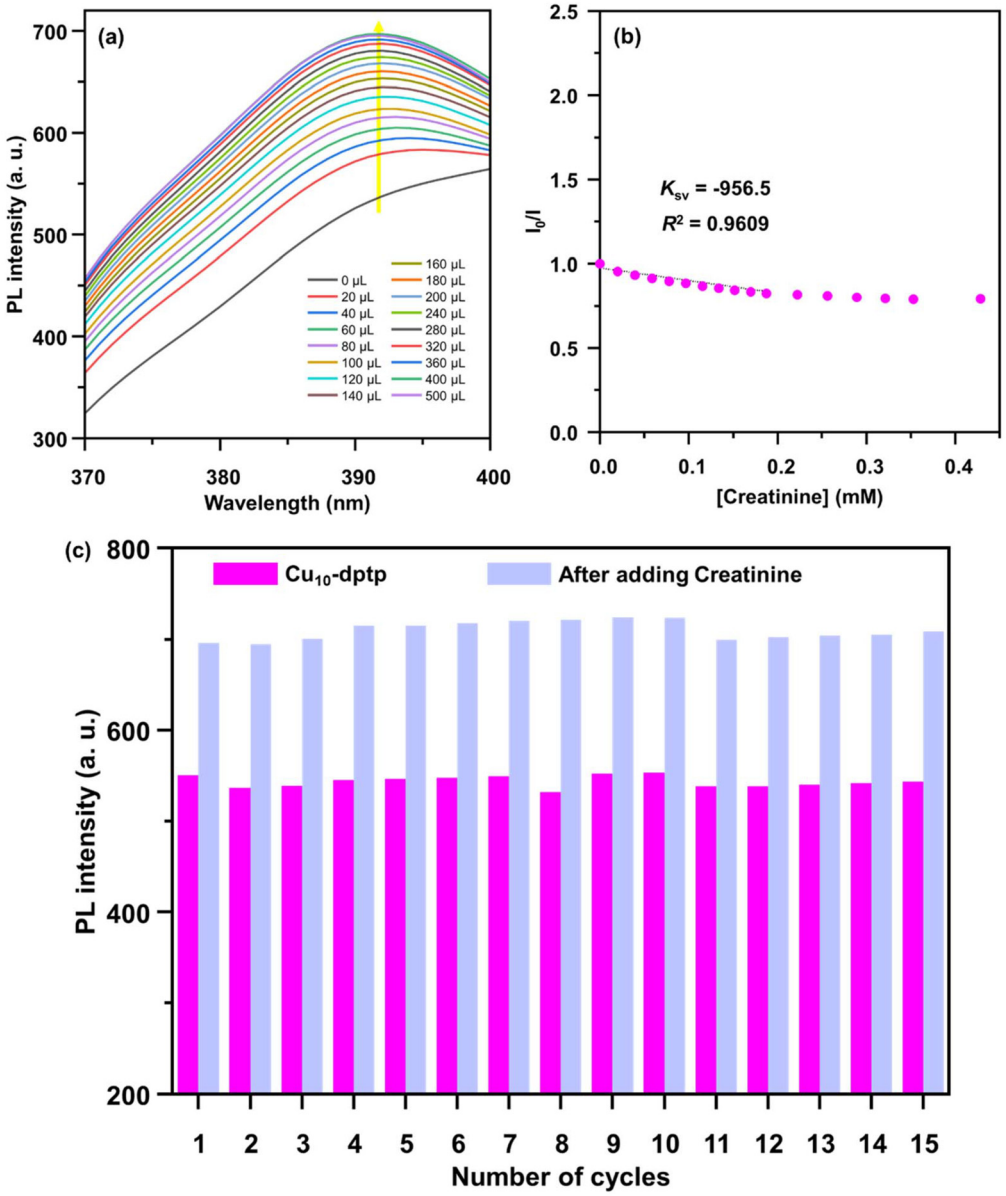

Fig. 7 (a) Concentration-dependent photoluminescence response of **Cu_{10}-dptp** to creatinine. (b) Stern–Volmer analysis illustrating fluorescence quenching behavior in aqueous media. (c) Reusability assessment of **Cu_{10}-dptp** over multiple creatinine sensing cycles.

tric environment. Creatinine acts here not as a quencher, but as a rigidity-inducing, non-coordinating modulator that suppresses nonradiative pathways by: (i) interacting with interlayer surfaces and reducing vibrational freedom, (ii) passivating defect sites and reducing excited-state trapping, and (iii) altering the microenvironment polarity to favor radiative decay. Thus, the presence of creatinine enhances luminescence, consistent with guest-induced suppression of nonradiative decay. The Stern–Volmer plot in this concentration window (1.98×10^{-5}–1.51×10^{-4} M) is well described by: $I_0/I = -956.5\ [Q] + 1.00$ ($R^2 = 0.9609$). The negative slope reflects an intensity-enhancing ("anti-quenching") response, where increasing analyte concentration increases I rather than decreases it. The magnitude $|K_{SV}| = 956.5\ M^{-1}$ is slightly larger than that of **Cu_{10}-bddi**, highlighting the strong environmental sensitivity of electronically coupled Cu(I) cluster states embedded within the flexible 2D π-framework. The larger LOD (4052 μM) arises because enhancement-type responses generally have higher noise-to-signal ratios than quenching-type ones. Together, these findings reveal how coordination topology, framework dimensionality, and cluster–ligand electronic coupling cooperatively define the sensing behavior of CCAMs. **Cu_{10}-bddi**, with its rigid 1D architecture and localized emissive states, functions as a creatinine-responsive fluorescence quencher with high Stern–Volmer sensitivity. **Cu_{10}-dptp**, with its electronically coupled Cu(I) clusters embedded in a π-rich 2D framework, demonstrating a distinct and complementary detection mechanism. This duality underscores the broader principle that reticular cluster design enables programmable photophysical responses, offering a versatile platform for chemical sensing in aqueous environments. Structurally, creatinine recognition in both CCAMs is expected to be dominated by reversible, noncovalent host–guest interactions rather than strong coordination to Cu sites. Given the polar functionality of creatinine (carbonyl and N–H groups) and the modest permanent porosity/interstitial free volume of **Cu_{10}-bddi** and **Cu_{10}-dptp**, the association can be rationalized as a combination of size-matching confinement within accessible voids (interchain/interlayer free volume) and hydrogen bonding (primarily with carboxylate O atoms and other heteroatom-rich regions in the ligand shell), with dipolar electrostatic interactions further stabilizing adsorption within the polar Cu–O-rich microenvironment. In **Cu_{10}-dptp**, additional surface/interlayer adsorption promoted by the π-extended dptp scaffold is also plausible. Notably, while the underlying binding mode is largely noncovalent and reversible in both materials, the opposite optical readouts (quenching *vs.* enhancement) arise from their distinct excited-state landscapes and microenvironments.

The long-term operational stability of luminescent sensors is a critical parameter for their practical deployment, particularly for aqueous analyte detection where repeated exposure to guest molecules can disrupt framework integrity or alter the emissive centers. To assess whether the copper cluster–assembled materials preserve their sensing capability over multiple uses, we carried out systematic recyclability studies for both **Cu_{10}-bddi** and **Cu_{10}-dptp** under identical creatinine detection conditions. For **Cu_{10}-bddi**, the emission intensity at 275 nm excitation was recorded over 15 consecutive sensing–regeneration cycles. After each cycle, the material was separated, washed thoroughly with water, and redispersed for the next measurement. Remarkably, the luminescence quenching response showed no measurable attenuation over all 15 cycles (Fig. 6c), indicating that neither the Cu_{10} cluster core nor the bddi linker environment undergoes photodegradation, ligand displacement, or Cu redox changes during analyte exposure. The robustness is attributed to the rigid one-dimensional chain architecture, in which the thiolate–carboxylate–coordinated $Cu(I)_{10}$ cluster nodes are sterically shielded by the bddi ligands and stabilized by a dense multidentate coordination shell, effectively suppressing ligand exchange and framework distortion during repeated guest adsorption–desorption. A similar evaluation was performed for **Cu_{10}-dptp**, which displays a turn-on luminescence response toward creatinine under 355 nm excitation. Across 15 repeated cycles, the emission enhancement factor remained virtually unchanged (Fig. 7c). This excellent recyclability reflects the intrinsic stability of the 2D Cu(I) cluster sheets, in which the $\{Cu_{10}S_6O_6N_4\}$ nodes are embedded within a rigid dptp-bridged lattice. The Cu(I) centers—being coordinatively saturated by thiolate, carboxylate, and pyridyl donors—do not participate in irreversible binding or oxidation during sensing, thereby maintaining their emissive properties over extended cycling. To verify that the preserved optical response arises from true structural retention rather than coincidental spectral similarity, we performed post-sensing FT-IR spectroscopy on both materials. For **Cu_{10}-bddi**, the FT-IR spectrum after 15 sensing cycles was virtually superimposable on that of the pristine sample (Fig. S17), with diagnostic vibrational signatures—including the C≡C stretching mode of the bddi linker, thiolate (ν(C–S)), and carboxylate (ν_{asym} and $\nu_{sym}(COO^-)$) modes—remaining unchanged within instrumental resolution. The absence of new bands (*e.g.*, ν(C=O) or ν(N–H) features from adsorbed creatinine) confirms that sensing proceeds *via* non-covalent, reversible interactions, without guest insertion or framework degradation. Likewise, **Cu_{10}-dptp** retained all characteristic vibrational bands following creatinine exposure (Fig. S18), including the pyridyl ν(C–N) stretches and the thiophene-based aromatic modes. No shifts or intensity changes indicative of ligand exchange, Cu–N bond cleavage, or framework rearrangement were detected. This observation, combined with the preserved luminescence behavior, demonstrates that creatinine sensing in **Cu_{10}-dptp** is also fully reversible and does not perturb the coordination environment of the Cu(I) cluster nodes. Collectively, these results highlight the exceptional stability, reusability, and structural fidelity of both cluster-assembled materials during creatinine detection. The ability to operate over many cycles without degradation underscores the intrinsic resilience of cluster-based reticular assemblies, where cooperative ligand fields and well-defined S/O/N coordination shells impart robustness comparable to that of classical MOFs while enabling rich photophysical responses suitable for aqueous biosensing applications.

Conclusions

In summary, we have demonstrated that atomically precise decanuclear copper clusters can be strategically integrated with organic linkers to generate structurally robust and compositionally tunable cluster-assembled materials spanning one and two dimensions. The 1D **Cu_{10}-bddi** and 2D **Cu_{10}-dptp** architectures arise from the controlled coordination of the same Cu_{10} secondary building unit, yet they manifest distinct electronic microenvironments—originating from differences in coordination connectivity, ligand field strength, and framework dimensionality within Cu(I)-based cluster nodes—which profoundly shape their optical responses in aqueous media. These structural divergences translate directly into contrasting luminescent sensing behaviors toward creatinine. **Cu_{10}-bddi** displays a sensitive fluorescence-quenching response with a Stern–Volmer constant of 885.1 M^{-1} and a limit of detection of 726 μM, whereas **Cu_{10}-dptp** exhibits creatinine-induced emission enhancement, characterized by a K_{SV} of −956.5 M^{-1} and a LOD of 4052 μM. Both materials retain their sensing performance over fifteen consecutive cycles, with FT-IR analyses confirming the preservation of their structural frameworks after repeated analyte exposure. These findings highlight how the dimensionality, coordination environment, and electronic structure of Cu_{10} cluster nodes can be leveraged to tailor analyte–framework interactions and photophysical responses. More broadly, this study establishes reticular cluster assembly as a powerful design principle for developing recyclable luminescent sensors and opens new avenues for atomically precise metal-cluster materials in aqueous chemical detection and functional optoelectronics.

Author contributions

S. D. and Y. N. conceived and supervised the research. T. I. and S. K. S. carried out the synthesis. R. N. and A. K. contributed to the SCXRD measurements and analysis. Material characterization was performed by T. I. and S. K. S. M. N. and T. K. contributed to the characterization. Application experiments were conducted by T. I. and K. S. The manuscript was prepared by S. D. All authors participated in data analysis and interpretation and approved the final version of the manuscript.

Conflicts of interest

There are no conflicts to declare.

Data availability

The data supporting this article have been included as part of the supplementary information (SI). Supplementary information is available. See DOI: https://doi.org/10.1039/d5nr05249a.

CCDC 2503061 and 2503062 ($[Cu_{10}(S^tBu)_6(CF_3COO)_4(bddi)_4]_n$ and $[Cu_{10}(S^tBu)_6(CF_3COO)_4(dptp)_4]_n$) contain the supplementary crystallographic data for this paper.[55a,b]

Acknowledgements

The authors thank Jin Sakai and Rina Tomioka (Tokyo University of Science) for their assistance with SCXRD measurements. This study was financially supported by the Scientific Research on Innovative Areas “Aquatic Functional Materials” (grant no. 22H04562), JSPS KAKENHI (grant no. 23H00289 and 23KK0098), the Yazaki Memorial Foundation for Science and Technology, and the FUSO Innovative Technology Fund.

References

1 Y. Du, H. Sheng, D. Astruc and M. Zhu, *Chem. Rev.*, 2020, **120**, 526–622.
2 P. Pan, X. Kang and M. Zhu, *Chem. – Eur. J.*, 2025, **31**, e202404528.
3 S. Li, N.-N. Li, X.-Y. Dong, S.-Q. Zang and T. C. W. Mak, *Chem. Rev.*, 2024, **124**, 7262–7378.
4 Q. Yao, Z. Wu, Z. Liu, Y. Lin, X. Yuan and J. Xie, *Chem. Sci.*, 2021, **12**, 99–127.
5 K. L. D. M. Weerawardene, H. Häkkinen and C. M. Aikens, *Annu. Rev. Phys. Chem.*, 2018, **69**, 205–229.
6 X. Kang and M. Zhu, *Chem. Soc. Rev.*, 2019, **48**, 2422–2457.
7 I. Chakraborty and T. Pradeep, *Chem. Rev.*, 2017, **117**, 8208–8271.
8 R. Jin, C. Zeng, M. Zhou and Y. Chen, *Chem. Rev.*, 2016, **116**, 10346–10413.
9 R. Jin, G. Li, S. Sharma, Y. Li and X. Du, *Chem. Rev.*, 2021, **121**, 567–648.
10 H. Hirai, S. Ito, S. Takano, K. Koyasu and T. Tsukuda, *Chem. Sci.*, 2020, **11**, 12233–12248.
11 S. Biswas, A. K. Das and S. Mandal, *Acc. Chem. Res.*, 2023, **56**, 1838–1849.
12 R. K. Gupta, Z. Wang, B. Mohan, C.-H. Tung and D. Sun, *Adv. Funct. Mater.*, 2025, 2507047.
13 H. Seong and D. Lee, *Bull. Korean Chem. Soc.*, 2024, **45**, 435–450.
14 L. He, T. Dong, D.-E. Jiang and Q. Zhang, *Coord. Chem. Rev.*, 2025, **535**, 216633.
15 S. Maity, S. Kolay, S. Chakraborty, A. Devi, Rashi and A. Patra, *Chem. Soc. Rev.*, 2025, **54**, 1785–1844.
16 P. D. Jadzinsky, G. Calero, C. J. Ackerson, D. A. Bushnell and R. D. Kornberg, *Science*, 2007, **318**, 430–433.
17 Y. Lu and W. Chen, *Chem. Soc. Rev.*, 2012, **41**, 3594–3623.
18 L. C. McKenzie, T. O. Zaikova and J. E. Hutchison, *J. Am. Chem. Soc.*, 2014, **136**, 13426–13435.
19 Z. Gan, J. Chen, J. Wang, C. Wang, M.-B. Li, C. Yao, S. Zhuang, A. Xu, L. Li and Z. Wu, *Nat. Commun.*, 2017, **8**, 14739.
20 M. Brust, M. Walker, D. Bethell, D. J. Schiffrin and R. Whyman, *J. Chem. Soc., Chem. Commun.*, 1994, 801–802.
21 X. Song, W. Zhu, X. Ge, R. Li, S. Li, X. Chen, J. Song, J. Xie, X. Chen and H. Yang, *Angew. Chem., Int. Ed.*, 2021, **60**, 1306–1312.

22 Y. Xie, Y. Xianyu, N. Wang, Z. Yan, Y. Liu, K. Zhu, N. S. Hatzakis and X. Jiang, *Adv. Funct. Mater.*, 2018, **28**, 1702026.
23 H. Ma, X. Zhang, L. Liu, Y. Huang, S. Sun, K. Chen, Q. Xin, P. Liu, Y. Yan, Y. Wang, Y. Li, H. Liu, R. Zhao, K. Tan, X. Chen, X. Yuan, Y. Li, Y. Liu, H. Dai, C. Liu, H. Wang and X.-D. Zhang, *Sci. Adv.*, 2023, **9**, eadh7828.
24 X. Yuan, Y. Tay, X. Dou, Z. Luo, D. T. Leong and J. Xie, *Anal. Chem.*, 2013, **85**, 1913–1919.
25 X. Yuan, T. J. Yeow, Q. Zhang, J. Y. Lee and J. Xie, *Nanoscale*, 2012, **4**, 1968–1971.
26 M.-M. Zhang, X.-Y. Dong, Z.-Y. Wang, H.-Y. Li, S.-J. Li, X. Zhao and S.-Q. Zang, *Angew. Chem., Int. Ed.*, 2020, **59**, 10052–10058.
27 N. K. Das, S. Ghosh, A. Priya, S. Datta and S. Mukherjee, *J. Phys. Chem. C*, 2015, **119**, 24657–24664.
28 X. Liu and D. Astruc, *Coord. Chem. Rev.*, 2018, **359**, 112–126.
29 A. Baghdasaryan and T. Bürgi, *Nanoscale*, 2021, **13**, 6283–6340.
30 M. Chen, C. Guo, L. Qin, L. Wang, L. Qiao, K. Chi and Z. Tang, *Nano-Micro Lett.*, 2025, **17**, 83.
31 Y. Liu, J. Yu, Y. Lun, Y. Wang, Y. Wang and S. Song, *Adv. Funct. Mater.*, 2023, **33**, 2304184.
32 S. Biswas, S. Das and Y. Negishi, *Nanoscale Horiz.*, 2023, **8**, 1509–1522.
33 S. Biswas and Y. Negishi, *J. Phys. Chem. Lett.*, 2024, **15**, 947–958.
34 Z.-Y. Wang and S.-Q. Zang, Chapter 16 - Coinage Metal Cluster-Assembled Materials, in *Atomically Precise Nanochemistry*, ed. R. Jin and D. Jiang, John Wiley & Sons Ltd, Chichester, 2023, pp. 479–501. DOI: 10.1002/9781119788676.ch16.
35 R. Nakatani, S. Das and Y. Negishi, *Nanoscale*, 2024, **16**, 9642–9658.
36 N. Alam, A. K. Das, P. Chandrashekar, P. Baidya and S. Mandal, *Nanoscale*, 2024, **16**, 10087–10107.
37 R.-W. Huang, Y.-S. Wei, X.-Y. Dong, X.-H. Wu, C.-X. Du, S.-Q. Zang and T. C. W. Mak, *Nat. Chem.*, 2017, **9**, 689–697.
38 Z.-Y. Wang, M.-Q. Wang, Y.-L. Li, P. Luo, T.-T. Jia, R.-W. Huang, S.-Q. Zang and T. C. W. Mak, *J. Am. Chem. Soc.*, 2018, **140**, 1069–1076.
39 M. J. Alhilaly, R.-W. Huang, R. Naphade, B. Alamer, M. N. Hedhili, A.-H. Emwas, P. Maity, J. Yin, A. Shkurenko, O. F. Mohammed, M. Eddaoudi and O. M. Bakr, *J. Am. Chem. Soc.*, 2019, **141**, 9585–9592.
40 J. Sakai, S. Biswas, T. Irie, H. Mabuchi, T. Sekine, Y. Niihori, S. Das and Y. Negishi, *Nanoscale*, 2023, **15**, 12227–12234.
41 R. Nakatani, S. Biswas, T. Irie, J. Sakai, D. Hirayama, T. Kawawaki, Y. Niihori, S. Das and Y. Negishi, *Nanoscale*, 2023, **15**, 16299–16306.
42 R. Nakatani, S. Biswas, T. Irie, Y. Niihori, S. Das and Y. Negishi, *ACS Mater. Lett.*, 2024, **6**, 438–445.
43 J. Sakai, K. Sasaki, R. Nakatani, S. Das and Y. Negishi, *Nanoscale*, 2024, **16**, 21767–21775.
44 T. Irie, K. Sasaki, M. Nozaki, T. Kawawaki, S. Takahashi, S. Das and Y. Negishi, *Nanoscale*, 2025, **17**, 25495–25504.
45 M. Cao, S. Wang, J.-H. Hu, B.-H. Lu, Q.-Y. Wang and S.-Q. Zang, *Adv. Sci.*, 2022, **9**, 2103721.
46 Y.-H. Li, R.-W. Huang, P. Luo, M. Cao, H. Xu, S.-Q. Zang and T. C. W. Mak, *Sci. China: Chem.*, 2019, **62**, 331–335.
47 A. K. Das, S. Biswas, S. S. Manna, B. Pathak and S. Mandal, *Inorg. Chem.*, 2021, **60**, 18234–18241.
48 Z. Liu, J.-J. Fang, Z.-Y. Wang, Y.-P. Xie and X. Lu, *Inorg. Chem.*, 2024, **63**, 11146–11154.
49 Y. Xu, Q.-G. Dong, J.-P. Dong, H. Zhang, B. Li, R. Wang and S.-Q. Zang, *Chem. Commun.*, 2023, **59**, 3067–3070.
50 Q.-Y. Wang, L. Zhang, W.-M. He, L. Yang, C. Zhang, Z.-Y. Wang, R. Zhang, J.-H. Chen, S. Wang, S.-Q. Zang and T. C. W. Mak, *Chem. Eng. J.*, 2020, **389**, 124455.
51 S. Das, J. Sakai, R. Nakatani, A. Kondo, R. Tomioka, S. Das, S. Takahashi, S. Biswas and Y. Negishi, *Chem. Sci.*, 2025, **16**, 2600–2608.
52 C. E. Turner and N. Gant, The biochemistry of creatine, in *Magnetic Resonance Spectroscopy*, 2014, pp. 91–103.
53 A. Nene, C. Phanthong, W. Surareungchai and M. Somasundrum, *J. Solid State Electrochem.*, 2023, **27**, 2869–2875.
54 C. Das, J. Raveendran, J. Bayry and P. A. Rasheed, *RSC Adv.*, 2024, **14**, 33784–33793.
55 (*a*) CCDC 2503061: Experimental Crystal Structure Determination, 2026, DOI: 10.5517/ccdc.csd.cc2q0mx9; (*b*) CCDC 2503062: Experimental Crystal Structure Determination, 2026, DOI: 10.5517/ccdc.csd.cc2q0myb.